

A deep autoencoder based approach for the inverse design of an acoustic-absorber

K. Mahesh^{1,3}, S. Kumar Ranjith² and R. S. Mini^{1*}

¹*Department of Mechanical Engineering, College of Engineering Trivandrum (Government of Kerala), Thiruvananthapuram, 695016, Kerala, India.

²Micro/Nanofluidics Research Laboratory, Department of Mechanical Engineering, College of Engineering Trivandrum (Government of Kerala), Thiruvananthapuram, 695016, Kerala, India.

³APJ Abdul Kalam Technological University, Thiruvananthapuram, 695016, Kerala, India.

*Corresponding author(s). E-mail(s): rsmmini@cet.ac.in;
Contributing authors: maheshnilambur2012@gmail.com;
ranjith@cet.ac.in;

Abstract

This paper proposes an algorithm to perform the inverse design of a low-frequency acoustic absorber using a deep convolutional autoencoder network. A hybrid sound-absorber configuration based on Helmholtz resonators with inserted curvy neck and microperforated panel is suggested and its geometrical properties are inversely forecasted from the targeted signal. A mathematical model is put forwarded to evaluate the absorption characteristics of the introduced geometry by employing the effective medium theory and the electro-acoustic analogy. The large dataset required to train, validate and test the deep neural network is extracted through this analytical procedure. Initially, the proposed inverse technique is successfully applied on a standard Helmholtz resonator based absorber setup with great accuracy. This prediction approach is further extended to suit the inverse design of a hybrid sound absorber with complex geometrical attributes. The encoder maps the input acoustic absorption spectrum to geometrical features of the absorber, and the subsequent decoder recreates the absorption characteristics using convolutional layers. Once the training and testing of the neural network are over, the deep autoencoder inversely predicts the geometrical parameters. In comparison with earlier inverse models which employed deep neural networks, the accuracy of the current scheme is

2 A deep autoencoder based approach for the inverse design of an acoustic-absorber

very high and no pre-design information on absorber geometry is required as well. Since the relevant learnable parameters involved are very low, the computational load is also very less for this autoencoder based method. Later, using the new inverse scheme, four representative absorber designs with specific acoustic functionality are deduced. Most importantly, these four compact absorber models produce quasi-perfect absorption in the frequency bands 200–315 Hz, 255–400 Hz, 300–530 Hz, and 350–650 Hz. Notably, the developed absorber versions have great potential in noise reduction applications owing to their deep sub-wavelength thickness ($\lambda/23$ at 200 Hz) and wide absorption spectra.

Keywords: Low frequency sound absorption, Helmholtz resonator, Analytical modelling, Electro-acoustic analogy, Convolutional autoencoder, Inverse design

1 Introduction

Rapid urbanization and industrialization are adversely affecting humans and other lifeforms through various environmental pollutions in general and noise pollution in particular. The mitigation and control of noise are critical in the modern era for the physical and mental well-being of all lifeforms [1–3]. The low-frequency noise generated by transportation vehicles, industrial machineries and aircrafts [4, 5] requires special attention due to its large operational wavelength. Often, passive absorbers, such as porous and fibrous materials are found to have limited applications owing to its intrinsic weakness in absorbing low-frequency noise [6] and inherent bulkiness [7]. Other potential low-frequency absorber candidates include resonant structures, such as Helmholtz resonator (HR) [8–11], quarter-wavelength resonators [12, 13], and microperforated panel (MPP) [14–16]. However, these resonant absorbers possess narrow absorption bands in low-frequency regime, thereby they are less suitable for acoustic applications [13, 14]. Thus, most of the traditional absorber configurations are curtailed either by their size or absorption bandwidth, which demands a detailed investigation to develop compact low-frequency sound absorbers.

With the advent of additive manufacturing techniques, several modifications are made on conventional MPPs [17–19] and HRs [20–22] to reduce their thickness without compromising the absorption performance. Guo et al. proposed Helmholtz resonator with extended [22] as well as spiral neck [23] configurations to improve low-frequency sound abatement with a minimum space consumption. However, these setups produced relatively narrow absorption bandwidth. Meanwhile, researchers experimented with alternative MPP topologies to expand the absorption spectra. To improve the low-frequency absorption, Wang et al. [18] developed a parallel array of MPP absorbers with varying cavity depths. Gai et al. [24] realized MPPs of L-shaped cavities to enhance absorption. Nevertheless, these models have long back cavities and that limit their engineering applications. Moreover, hybrid structures such as MPP backed by HR [25] and MPP combined with coiled-up cavities [26] are proposed to promote absorption in the low-frequency regime. Similarly, Boccaccio et al. [27] attempted a hybrid absorber of MPP and Archimedean-inspired spiral configuration, to attenuate noise in the low-mid frequency range, however the complexity

of the structure has elevated. Recent studies suggest that a parallel configuration of MPP and multiple Helmholtz resonators with inserted neck (HRIN) mitigated disadvantages of previous designs [28, 29]. This absorber structure is compact, sturdy, simple to manufacture, and has broadband low-frequency absorption capabilities. Note that, the proposed configuration, absorbed more than 90% of the acoustic waves in the frequency span of 347–630 Hz. Still, there is enough room to design a compact absorber by further shifting the absorption regime to the lower side. In this regard, a novel absorber model is proposed in this investigation, for low-frequency acoustic absorption by agglomerating MPP and HR. Most importantly, this configuration inherits numerous tunable geometrical features and optimal dimensions of the absorber needed to be inversely speculated.

Inverse prediction strategies are versatile, powerful and widely adopted to solve numerous scientific and engineering problems [30, 31]. The traditional optimization strategies such as genetic algorithms [32, 33], particle swarm optimization [34] and topology optimization [35], are constrained with its computationally inefficient random search nature and the possibility to quickly fall into saddle points or local optima [36, 37]. Moreover, the computational complexity grows as the absorber design becomes more sophisticated [38–40]. Besides these, the traditional optimization approach lacks the benefits of on-demand design, which is indeed essential for an efficient inverse design [41, 42]. In this context, the inverse design based on deep neural networks (DNN) assumes importance as it is a promising method that circumvents all these shortcomings [29]. Typically, this data-driven artificial intelligence technique is employed in almost all the research domains [43–46]. In particular, inverse design problems in nanophotonics [47–49], airfoils [50], optics [51], nano-materials [52] and electromagnetic absorbers [39, 41] are successfully solved using DNN methods. Similarly, for acoustics, the forward problems such as prediction of absorption characteristics of broom fibers [53] and layered fibrous material [54] are attended using DNN. In contrast, deep learning techniques are rarely deployed for the inverse prediction problems in acoustics [29, 33, 42].

In this context, the inverse design using the deep neural network (IDDN) technique that developed previously demands special attention [29]. Indeed, the proposed IDDN efficiently mapped the relation between absorption spectra and geometrical parameters. However, it required a priori information regarding any of the geometric features of the absorber apart from the absorption coefficient to forecast and optimize the remaining geometrical dimensions. Perhaps, it is a complex constraint, which inevitably reduces the flexibility of the design process. This trade-off may be circumvented using improved neural network design like a convolutional autoencoder. It is noteworthy that, autoencoder is a type of DNN architecture which is predominantly used for unsupervised learning processes, such as dimensionality reduction [55], image processing [56], anomaly detection [57, 58], machine translation [59], and so on. Autoencoders are generally applied in acoustics for speech enhancement and acoustic novelty detection applications [60]. Moreover, autoencoder has been demonstrated as an excellent tool for the inverse design problems in various disciplines of physics and engineering [41, 61–63]. Typically, an autoencoder comprises of two parts: an encoder that maps input data to a latent representation

4 A deep autoencoder based approach for the inverse design of an acoustic-absorber

and a decoder that reconstructs the same input data from this compressed representation [64]. Both of these segments are learned concurrently during neural network training to obtain the forward and inverse mapping between input and latent space. This synergistic learning feature of autoencoders avoids the non-uniqueness issue of inverse designs [41, 65]. Thereby, extending convolutional autoencoder based inverse design to construct an acoustic-absorber is expected to be a promising approach.

Data-driven methods in general and DNN-based inverse design in particular requires large-sized dataset for neural network training. Often, this data can be obtained through numerical or analytical or experimental techniques. However, for the majority of acoustic applications, the data generation through numerical or experimental means is impractical owing to resource limitations. Therefore, the dataset creation for most of the reported inverse problems in acoustics was carried out by deploying analytical schemes [29, 33, 42, 66]. Perhaps, the absorber configuration under consideration consists of multiple HRs and MPP, and the electro-acoustic analogy-based analytical technique is suited well for data production [25, 28, 67]. The electro-acoustic analogy is developed based on the lumped parameter method, in which the acoustic components are assumed to behave similar to that of standard electrical components. Note that, this theory is only valid if the wavelength of the acoustic wave is significantly larger than the characteristic dimensions of the acoustic system [68, 69]. Since the proposed absorber configuration satisfies these conditions, an electro-acoustic analogy can be developed and deployed to generate the requisite dataset.

In summary, it is noted that, even though having a great design potential, autoencoder-based inverse schemes are rarely employed in acoustics. Specifically, convolutional autoencoder-based inverse design approaches are yet to find application in the development of complex hybrid absorbers. Furthermore, an analytical representation of the absorption characteristics of the proposed absorber with HR and MPP needs to be derived. In order to address all these deficiencies, the following objectives are identified for the current investigation.

- To propose a novel hybrid acoustic configuration based on MPP and Helmholtz resonator with inserted curvy neck (HRICN) having minimal thickness for low-frequency sound absorption.
- To develop a new mathematical model to evaluate the absorption properties of the introduced absorber using effective medium method and electro-acoustic analogy.
- To originate a new inverse design method to forecast the optimal geometrical features of the proposed compact absorber employing a convolutional autoencoder network.

In this investigation, a novel low-frequency acoustic-absorber model of MPP and multiple Helmholtz resonators with inserted curvy neck (HRICNs) is presented to shift the absorption peaks to lower frequencies without affecting the overall thickness of the structure. Thereafter, the convolutional autoencoder network-based inverse design technique is presented and applied to a standard absorber. Finally, using the novel inverse design scheme, the optimal design parameters of the proposed hybrid absorber are inversely speculated.

The overall algorithmic workflow of the present study is as follows:

1. Firstly, suggest a suitable acoustic-absorber geometry based on MPP and HRICNs to mitigate the low-frequency sound waves. (Section 2)
2. Develop a mathematical model to estimate the absorption response with respect to frequency for the proposed geometry by employing electro-acoustic analogy. (Section 2)
3. Deploy full-field finite element simulations using COMSOL Multiphysics to validate the proposed analytical approach. (Section 2)
4. Construct an inverse design architecture using the convolutional autoencoder network to forecast the geometric features of the acoustic-absorber from a desired acoustic functionality. (Section 3)
5. Apply the new inverse design strategy on a standard Helmholtz resonator based absorber to validate its accuracy and compare its performance with the previously demonstrated IDDN technique. (Section 3)
6. Extend the proposed inverse design scheme to a more complicated hybrid absorber by producing a large dataset for the neural network using the developed analytical solution and optimize its geometric features. (Section 4)

2 Design of a compact low-frequency acoustic-absorber

The major intention of the present examination is to create a low-frequency absorber with minimal thickness and broad absorption spectra. In this regard, the geometry design of the absorber, its analytical modelling and numerical validation are presented in this section.

2.1 Geometric construction of parallel-conjunction of MPP and multiple HRICNs (MHRICN)

In the previous works of authors', a parallel combination of MPP and HRINs (P-MPPHR) was developed, and this compact absorber demonstrated excellent low-frequency (347–630 Hz) absorption characteristics [28, 29]. However, there is a requirement to develop absorbers that has applicability in frequencies much lower than this range without increasing the total thickness of the absorber. For this purpose, a new hybrid acoustic configuration consisting of MPP and HRICN is presented here. All the long HRIN in the previous configuration [28, 29] are replaced with short HRICNs as shown in Fig. 1a. Here, the proposed absorber is a parallel-conjunction of MPP and four HRICNs (MHRICN). The physical model and the top view of MHRICN are given in Figs. 1a and 1b respectively and all the geometric parameters are clearly indicated. The schematic diagram of HRICN is shown in Fig. 1c where l_N denotes the neck length, d_N denotes the neck diameter, l_C denotes the cavity length and d_C denotes the cavity diameter. In HRICN, the neck is in the form of a curved channel and thus can be extended to a larger length without increasing the cavity depth. This enables designers to create acoustic-absorbers with extremely low resonance frequencies and minimum thickness [20]. Meanwhile, MPP can absorb noise

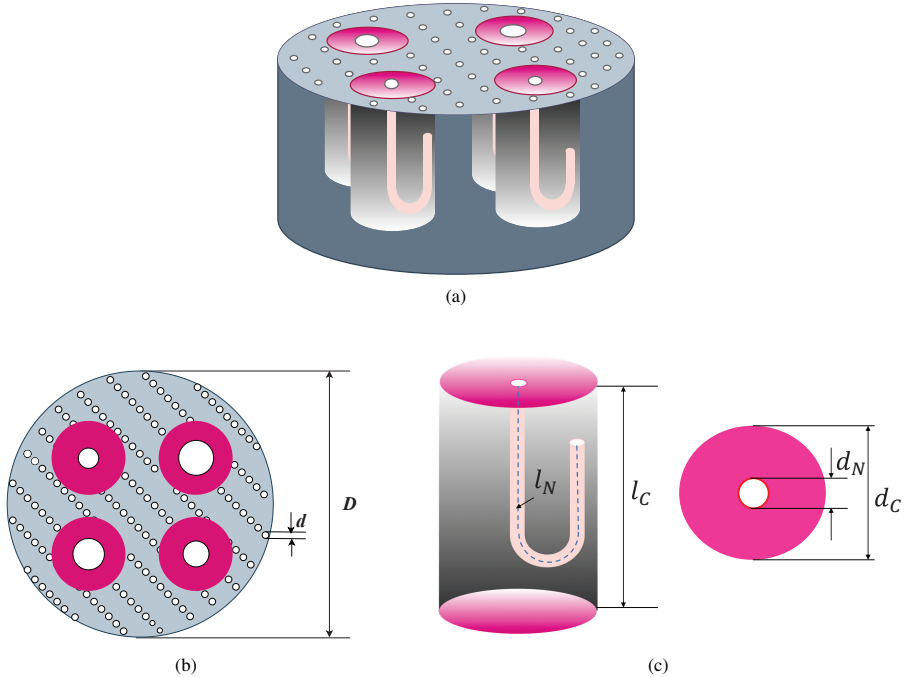


Fig. 1: Details of the proposed MHRICN configuration, (a) physical model and (b) top view of MHRICN, where d is the hole diameter of MPP and D is the outer diameter of MHRICN. (c) Schematic representation of HRICN subunit, where l_C is the cavity length, l_N is the neck length, d_N is the neck diameter and d_C is the cavity diameter.

over a wide range of frequencies [16, 28]. Thereby, this co-planar combination of HRICN with MPP is expected to facilitate broadband low-frequency noise reduction.

2.2 Mathematical modelling of absorption characteristics of MHRICN

In this section, the mathematical formulation of the sound absorption characteristics of the MHRICN is presented. This robust analytical prediction model is developed using effective medium method and electro-acoustic analogy. The schematic representation of parallel configuration of MPP and HRICNs is given in Fig. 2a. Based on the equivalent electro-acoustic circuit given in Fig. 2b, the acoustic impedance (Z_A) of MHRICN with ‘n’ number of HRICNs can be formulated as [68],

$$Z_A = \frac{1}{\frac{S_m}{Z_{MPP}+Z_C} + \sum_{i=1}^n \frac{S_i}{Z_{HRi}}}, \quad (1)$$

where $S_i = A_i/(\pi D^2/4)$ is the area ratio of i^{th} HRICN. Note, A_i is the area of single HRICN and D is the diameter of MHRICN and hence the area ratio of MPP is $S_m =$

$1 - \Sigma S_i$. In addition, Z_{HR} and Z_{MPP} are acoustic impedance of HRICN and MPP respectively. The detailed derivation of Z_{HR} is summarized in Appendix A. Further, the specific acoustic impedance of MPP (Z_{MPP}) as well as backing cavity (Z_C) are represented as [14],

$$Z_{MPP} = z_0 (R_{MPP} + jX_{MPP}) \quad (2)$$

and

$$Z_C = -jz_0 \cot(kl_p). \quad (3)$$

Here, z_0 is the impedance of air, l_p is the backing cavity length of MPP, R_{MPP} is the normalized specific acoustic resistance and X_{MPP} is the normalized specific acoustic reactance [14]. Furthermore, R_{MPP} and X_{MPP} can be written as [14],

$$R_{MPP} = \frac{32\eta}{\sigma\rho cd^2} \left(\sqrt{1 + \frac{k_m^2}{32}} + \frac{\sqrt{2}}{8} k_m \frac{d}{t} \right) \quad (4)$$

and

$$X_{MPP} = \frac{\omega}{c} \frac{t}{\sigma} \left(1 + \frac{1}{\sqrt{9 + k_m^2/2}} + 0.85 \frac{d}{t} \right) \quad (5)$$

where, $k_m = (d/2) \sqrt{\rho\omega/\eta}$ is the perforate constant, c is the velocity of sound in air, ρ is the density of air, η is the dynamic viscosity of air, ω is the angular frequency and t, d and σ are the panel thickness, hole diameter and porosity respectively. Finally, from Z_A , the required absorption coefficient of MHRICN is obtained as,

$$\alpha = 1 - \left| \frac{Z_A - z_0}{Z_A + z_0} \right|^2. \quad (6)$$

2.3 Numerical modelling of MHRICN

This section describe about the full-field finite element simulations performed using COMSOL Multiphysics software. The multiphysics feature which combines the pressure acoustics and thermo-viscous models is used for the present numerical study. Under frequency domain interface, the propagation of sound through the waveguide and absorber is solved using the Helmholtz equation, which can be written as [70]:

$$\nabla \cdot \left(-\frac{1}{\rho} \nabla p \right) - \frac{\omega^2 p}{\rho c^2} = 0, \quad (7)$$

where p is the acoustic pressure.

The impedance tube model used for the numerical analyses is given in Fig. 3a, where the MHRICN absorber is placed at the right end. A two-microphone impedance tube model which is similar to an actual experimental setup is used for the investigation. The left end of the impedance tube is excited by a plane harmonic wave, where a matched boundary condition is applied. All other boundaries of the waveguide and absorber section are assigned as sound hard boundaries. Inside the

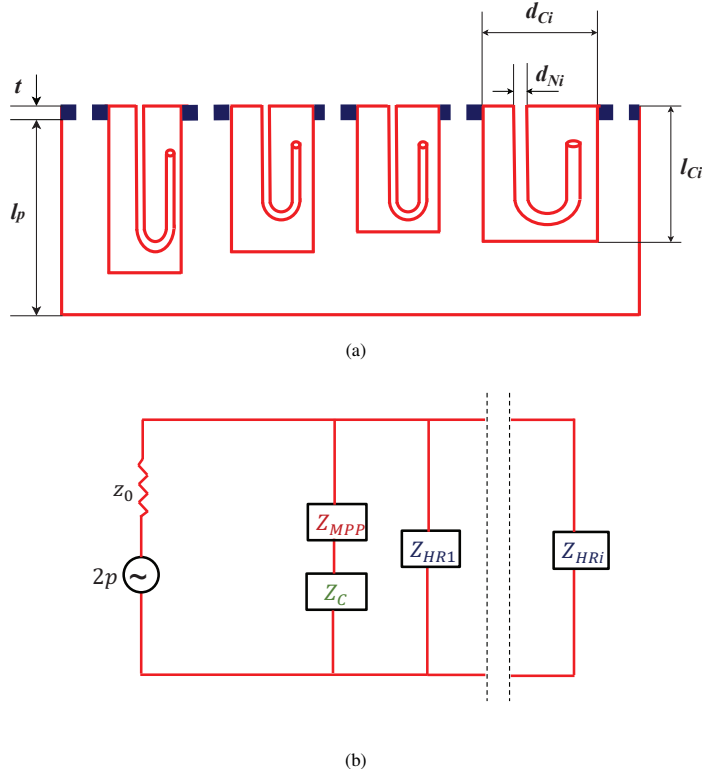


Fig. 2: (a) The schematic representation of MHRICN, where l_{Ci} is the cavity length, d_{Ni} is the neck diameter and d_{Ci} is the cavity diameter of i^{th} HRICN (i is the index number which varies from $n=1$ to 4). Further, d , t and l_p are the hole diameter, panel thickness and cavity depth respectively of MPP. (b) Equivalent electro-acoustic circuit, where Z_{HRI} is the acoustic impedance of the i^{th} HRICN, Z_{MPP} and Z_C are the acoustic impedance of MPP and backing cavity respectively.

absorber section as well as waveguide, air is chosen as the transmitting fluid medium for acoustic waves. The interior perforated plate condition is used to simulate the acoustic behaviour of MPP. Further, to accurately assess the thermo-viscous losses inside the HRICN's curved neck, the thermoacoustic feature is employed. For this, the continuity equation, linearized Navier-Stokes equation and energy equation are solved in the frequency domain. The set of governing equations numerically solved in the thermoviscous acoustic domain, by assuming a viscous compressible Newtonian fluid, are as follows [71],

$$j\omega\rho\left(\frac{p}{P_0} - \frac{T}{T_0}\right) + \rho\nabla \cdot \mathbf{v} = 0, \quad (8)$$

$$j\omega\rho\mathbf{v} = \nabla \cdot \left(-p + \eta(\nabla\mathbf{v} + (\nabla\mathbf{v})^T) - \frac{2}{3}\eta\nabla \cdot \mathbf{v}\right), \quad (9)$$

$$j\omega p C_p T = -\nabla \cdot (-K\nabla T) + j\omega p, \quad (10)$$

where \mathbf{v} and T denote fluid velocity and temperature respectively. Further, the heat capacity of air at constant pressure is denoted as C_p , and thermal conductivity is designated as K . Furthermore, P_0 and T_0 denote the equilibrium pressure and temperature respectively. The pressure responses corresponding to the frequency of interest are evaluated and further calculations are performed as per ISO-10534 standards [72]. Subsequently, the reflection coefficient (R) is calculated as

$$R = \frac{H_{12} - e^{-jks}}{e^{jks} - H_{12}} e^{2jkx_1}, \quad (11)$$

where H_{12} is the transfer function, which is the ratio of pressure response of microphone 2 to microphone 1, s is the distance between the microphones and x_1 is the distance from the first microphone to the absorber. Then the absorption coefficient (α) is estimated as

$$\alpha = 1 - |R|^2. \quad (12)$$

2.4 Comparison of theoretical and numerical results

The absorption properties of MHRICN with four inhomogeneous resonators are analyzed using both the analytical and numerical schemes. The diameter and length of cavity of all HRICNs are set as 30 mm and 50 mm respectively. Further the neck length is set as 80 mm for all HRs while neck diameters are fixed as 7, 8, 9 and 10 mm. Dimensions of MPP are set as $t = 1$ mm, $d = 0.4$ mm, $\sigma = 1.4\%$, $l_p = 50$ mm, and $D = 100$ mm. Comparison of absorption characteristics obtained from analytical and numerical schemes is depicted in Fig. 3b. Here, MHRICN exhibited five absorption peaks. Among them, the four low-frequency peaks respectively at 200 Hz, 230 Hz, 265 Hz and 300 Hz belong to the HRICNs, while the broadband peak around 657 Hz belongs to the MPP. The corresponding impedance spectra are depicted in Fig. 3c, where the resistive ($\text{Re}(Z_A/z_0)$) and reactive ($\text{Im}(Z_A/z_0)$) parts of normalized impedance are plotted. Note that, at impedance matching condition, the value of normalized resistive impedance is unity and the reactive impedance is zero [21, 22]. The given MHRICN model does not exhibit perfect absorption at any of the resonance frequencies. However, the absorber demonstrated near-perfect absorption at 265 Hz, 300 Hz, and 657 Hz. At these frequencies, the real component of normalised impedance is near to 1 and the imaginary part is equal to 0. However, at 200 Hz and 230 Hz, the real and imaginary values of normalised impedance are more deviated from 1 and 0 respectively. From Fig. 3b, it is demonstrated that the developed mathematical model is in excellent accord with the full field numerical simulations. Consequently, the simple and fast analytical predictions can be effectively used to replace the resource intensive full-field numerical simulations. Finally, to gain a deeper understanding on the absorption mechanism of the MHRICN, the reflection coefficients corresponding to the complex frequency domain ($f_c = f_{Re} + jf_{Im}$) are computed and plotted in Fig. 3d. For a hypothetical lossless system, the pairs of zeros and poles are complex conjugates and these are symmetrically distributed with respect to a real frequency axis ($f_{Im} = 0$). However, when visco-thermal losses are introduced into the system,

the leakage energy due to radiation effect gets balanced, and the zero point is shifted to the real frequency axis [73]. As shown in Fig. 3d all zeros are close to the real axis, which essentially demonstrates a near perfect absorption characteristics.

3 Inverse design of absorber using convolutional autoencoder network

It is noteworthy that the broadband absorption characteristics and reduced thickness of MHRICN is very much promising for an effective sound absorber. However, in order to maximize the absorption efficacy of MHRICN, its dimensions need to be properly identified. For this purpose an inverse design strategy is an apt choice, which can provide appropriate design parameters corresponding to targeted absorption properties. Indeed, inverse design based on deep neural network (IDDN) proposed in previous study [29] is an ideal candidate for inverse problems. However, in order to cope with complicated acoustic designs, IDDN requires further improvements. By introducing much advanced convolutional autoencoder network for inverse design, a drastic improvement in IDDN is expected. Compared to conventional techniques of optimization or inverse designs, IDDN is superfast and it provides feasible solutions with high fidelity. Whenever an absorption spectrum of desired functionalities is given as the input, the IDDN provides the corresponding design parameters as the output. However, due to the architectural constraint of the IDDN scheme, it requires additional information about the geometry of the absorber for accurate prediction of the remaining geometric parameters. Thus, the IDDN receives absorption spectra along with a geometric feature for the inverse design, that limits its flexibility. In this work, this particular limitation is subdued by proposing a novel architecture using convolutional autoencoder network.

3.1 Architecture of autoencoder based inverse design

An autoencoder consists of two building blocks, an encoder and a decoder. The encoder compresses an input data into an abstract form and a decoder reconstructs an output from this, consequently the input and the output are identical [74–76]. At first, the encoder (B) maps the given input layer $X \in \mathcal{R}^d$ to the abstract form $H \in \mathcal{R}^l$. This latent space is formulated as,

$$H = B_\phi(X), \quad (13)$$

where ϕ is the collection of all parameters of encoder model. Then, the decoder model (Γ) maps the abstract form $H \in \mathcal{R}^l$ to the output layer $X' \in \mathcal{R}^d$ in a reverse fashion. The output of decoder is formulated as,

$$X' = \Gamma_\zeta(H), \quad (14)$$

where ζ is the collection of all parameters of decoder model.

In this work, the autoencoder is used to regenerate the required absorption coefficients ($\hat{\alpha}$) from a desired absorption coefficients (α). In between, an intermediate

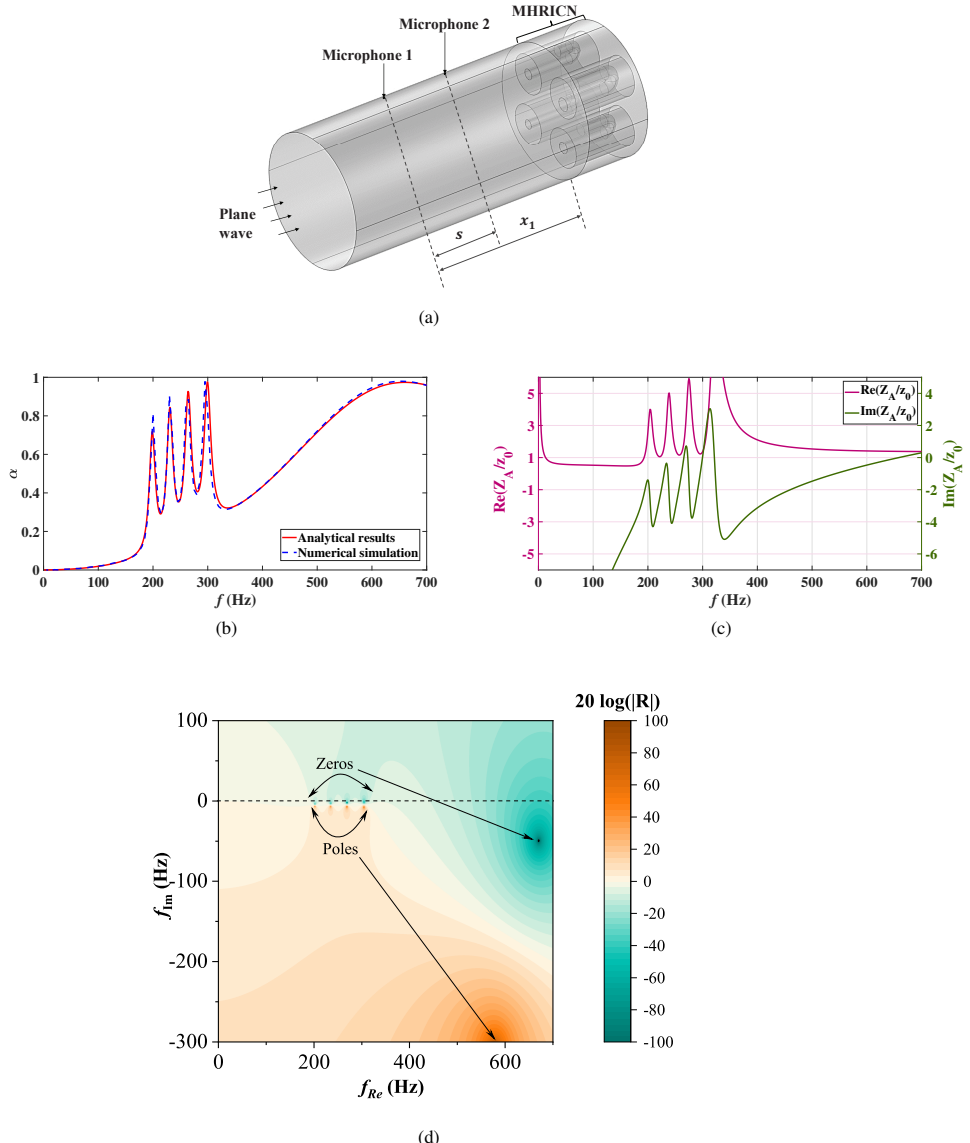


Fig. 3: (a) Numerical model of MHRICN absorber placed inside an impedance tube. (b) Numerical and analytical absorption characteristics of MHRICN and (c) its normalized resistive ($\text{Re}(Z_A/z_0)$) and reactive ($\text{Im}(Z_A/z_0)$) impedance. (d) The complex frequency plane representation of the MHRICN absorber. The dimensions of MHRICN are chosen as $l_{Ni}=80$ mm, $l_{Ci}=50$ mm, $d_{Ci}=30$ mm, $d_{N1}=7$ mm, $d_{N2}=8$ mm, $d_{N3}=9$ mm and $d_{N4}=10$ mm, where i is the index number of HRICN which varies from 1 to 4 and the dimensions of MPP are $d=0.4$ mm, $t=1$ mm, $\sigma=1.4\%$, $l_p=50$ mm and $D=100$ mm.

layer is incorporated to extract the geometric parameters from a desired absorption spectra. A schematic depiction of the developed inverse design using convolutional autoencoder network (ICAN) is given in Fig. 4. Here, the encoder receives desired absorption coefficients corresponding to the frequency of interest as the input and an intermediate layer which acts as the abstract form provides the geometric parameters of the absorber as the output. The decoding block, kept after the encoding block, reconstructs the absorption coefficients from the geometric parameters. In this study, the frequency of interest chosen is the low-mid frequency range of 0 - 700 Hz. Thus, the absorption coefficients corresponding to this frequency range is given as the input. Due to the one dimensional nature of the input, 1D convolutional layers are used for initial feature extraction. The encoder composes five 1D convolutional layers, after each convolutional layer max pooling layers are used to reduce the dimension of feature maps, see Fig. 4. Thereby, the max pooling layers reduce the amount of computational load and variance. The output of convolutional blocks is flattened into a single long feature map. Then this feature map is passed through four dense layers before acquiring the output of the encoder. In between dense layers, a dropout-layer is used to regularize the model, which in turn mitigate the overfitting scenario. Finally, geometric parameters of the absorber are obtained as the output of the encoding block.

Thereafter, the decoding block reconstructs the absorption coefficients from these geometric parameters by means of a reverse process. Initially the predicted geometric parameters are transformed into a long feature map using a couple of dense layers. After that, the feature map is passed through convolutional blocks of four 1D convolutional layers and three upsampling layers, see Fig. 4. While passing through the upsampling layers, the size of feature maps are doubled, which can be referred as an inverse operation of aforementioned max pooling function. Finally, the estimated absorption coefficients ($\hat{\alpha}$) are acquired as decoder output through a 1D convolutional layer of filter size one.

For the output layer of geometric parameters, a linear activation function is used. All other convolutional and dense layers are activated by rectified linear activation function (ReLU). The detailed description of different convolutional layers used for encoder and decoder in ICAN architecture is given in Table 1. The autoencoder model is trained for 500 epochs with Adam optimizer and the batch size is selected as 500. The learning rate is scheduled by cosine annealing method [77] with a restart learning rate of 0.001. A customized loss function is chosen for training as well as testing and is expressed as,

$$L(y_{i,j}, \hat{y}_{i,j}, \alpha_{i,k}, \hat{\alpha}_{i,k}) = \frac{1}{n} \sum_{i=1}^n \frac{1}{m} \sum_{j=1}^m |y_{i,j} - \hat{y}_{i,j}| + \beta \frac{1}{n} \sum_{i=1}^n \frac{1}{p} \sum_{k=1}^p |\alpha_{i,k} - \hat{\alpha}_{i,k}|, \quad (15)$$

where $\alpha_{i,k}$ and $\hat{\alpha}_{i,k}$ are the actual and the predicted absorption coefficients. Further, $y_{i,j}$ is the actual geometric parameter, $\hat{y}_{i,j}$ is the predicted geometric parameter, here, ‘ m ’ is the number of geometric parameters, ‘ p ’ is the number of absorption coefficients and ‘ n ’ is the number of data samples. Further, β is a hyperparameter which is selected as 0.005. For all investigations detailed in this work, the aforementioned

Table 1: The details of the convolutional neural network of the proposed ICAN model. Output 1 refers to the forecasted geometric parameters, and Output 2 represents the forecasted absorption coefficients.

No	Layer Type	Layer Details	Output Shape	Parameters
Encoder				
1	Conv 1D	16×3, Strides=1, Input shape = (700, 1)	698×16	64
2	MaxPooling 1D	Pool size=2, Strides=2	349×16	0
3	Conv 1D	32×3, Strides=1	347×32	1568
4	MaxPooling 1D	Pool size=2, Strides=2	173×32	0
5	Conv 1D	64×3, Strides=1	171×64	6208
6	MaxPooling 1D	Pool size=2, Strides=2	85×64	0
7	Conv 1D	128×3, Strides=1	83×128	24704
8	MaxPooling 1D	Pool size=2, Strides=2	41×128	0
9	Conv 1D	256×3, Strides=1	39×256	98560
10	MaxPooling 1D	Pool size=2, Strides=2	19×256	0
11	Flatten	...	4864	0
12	Dense	1024	1024	4981760
13	Dense	1024	1024	1049600
14	Dense	1024	1024	1049600
15	Dropout	Rate=0.2	1024	0
16	Dense	4 (Output 1)	4	4100
Decoder				
17	Dense	1024	1024	5120
18	Dense	95	95	97375
19	Reshape	...	95×1	0
20	Conv 1D	128×5, Strides=1	91×128	768
21	UpSampling 1D	Pool size=2, Strides=2	182×128	0
22	Conv 1D	64×5, Strides=1	178×64	41024
23	UpSampling 1D	Pool size=2, Strides=2	356×64	0
24	Conv 1D	32×5, Strides=1	352×32	10272
25	UpSampling 1D	Pool size=2, Strides=2	704×32	0
26	Conv 1D	1×5, Strides=1 (Output 2)	700×1	161

loss function and hyperparameters are consistently used. The iterative procedure of ICAN algorithm is depicted as a pseudocode in Fig. 5. Note, the iterative training operation of ICAN is terminated when the test-loss falls below 1×10^{-3} . The training and testing processes of deep learning models are carried out on Google Colaboratoy platform. The platform provided 2.3 GHz Intel Xeon processor and NVIDIA Tesla T4 GPU with 12 GB RAM. The neural network architectures are developed using Tensorflow 2.6.0 libraries complied with Python 3.7.11. Next, this ICAN network is implemented on a standard absorber to inversely predict the geometrical features.

3.2 Inverse design of a single HRICN absorber

Initially, ICAN scheme is deployed to inversely design a standard HRICN absorber, which is simple in construction as shown in Fig. 1c. Often, for any deep neural network based technique, a large dataset is essential to solve forward as well as inverse problems [29]. In the case of absorbers, generation of sufficient data using experimental or numerical means is a practically challenging task. Hence, the analytical

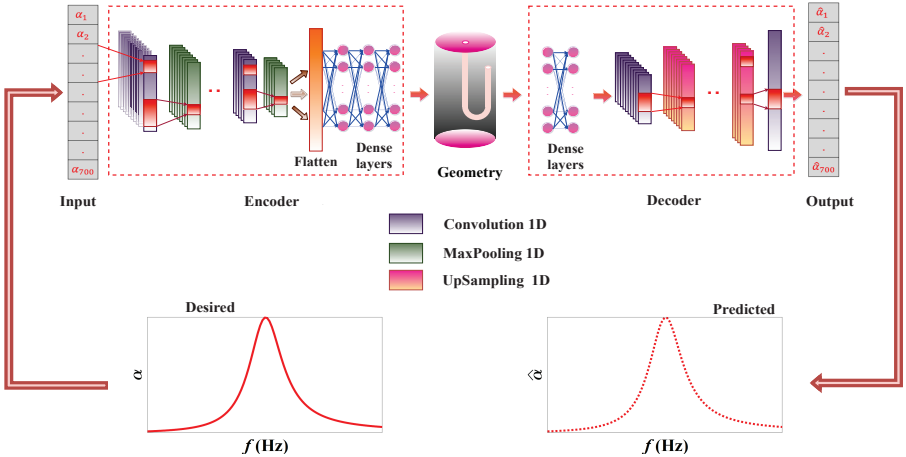


Fig. 4: Schematic representation of ICAN architecture. The desired absorption spectra serving as the encoder network's input, and the decoder network framed to map the relationship between estimated geometric parameters and estimated absorption spectra.

Table 2: The dimensions selected for data production in order to forecast the geometrical features of single HRICN absorber.

Parameters	Range of values (mm)
l_N	1 - 100
r_N	1 - 11
l_C	10 - 100
r_C	11 - 50

methodology discussed in Appendix A is used for the data generation in this work. The geometric parameters which defines the absorption spectra of HRICN are l_N , r_N , l_C and r_C (see Fig. 1c). Using Python programmes, the absorption spectra corresponding to a random collection of these four geometric parameters are created for a frequency range of 0 - 700 Hz using Eq. 27. The random values of geometric parameters are taken from a uniform distribution with a precision level of four significant digits. Note that, during the data preparation, all other geometric and material properties are kept constant. The selection of geometric parameters for the dataset creation is detailed in Table 2. An excerpt from the generated dataset is given in Fig. 6a, and it is evident that the absorption spectra are differed by the absorption peak and its resonance frequency depending on the input geometrical features. The main advantage is that, a large amount of data is generated from a wide spectrum of input geometries with limited computational resources.

For the inverse design of HRICN, a total of 320000 samples are created and 20% of the samples are then assigned for validation. The ICAN method is employed in HRICN to map the relationship between absorption coefficients and the four geometric parameters, l_N , r_N , l_C , and r_C . Indeed, the output of the encoder network in the

Generate dataset

Split dataset into Train/Validation and Test

Create deep autoencoder network

loop

Function ICAN TRAINING (e, h, α, l, θ)

$\alpha = [\alpha_1, \alpha_2, \dots, \alpha_n] \in R^{m \times n}$ is the input matrix, in which $\alpha_i \in [0, 1]^m (1 \leq i \leq m)$

e is the number of epochs

q is the number of batches

l is the learning rate

$\theta = \{\phi, \zeta\}$ are the parameters of the autoencoder network

for $a=0$ to e **do**

for $b=0$ to q **do**

$\hat{y} = B_\phi(\alpha)$

$\hat{\alpha} = \Gamma_\zeta(\hat{y})$

 compute loss ($L(y, \hat{y}, \alpha, \hat{\alpha})$) which is defined in Eqn. 15

g = compute the gradient of loss with respect to θ

for θ_i, g_i in (θ, g) **do**

$\theta_{i+1} = \theta_i - l * g_i$

end for

end for

end for

end Function

compute loss on test set ($(L_{\text{test}}(y, \hat{y}, \alpha, \hat{\alpha}))$)

if $(L_{\text{test}}(y, \hat{y}, \alpha, \hat{\alpha})) < \text{tolerance}$

 save autoencoder model

end loop

else go for

 update autoencoder network with suitable layers and layer parameters

end if

end loop

Deploy trained model to predict geometric parameters

Fig. 5: Pseudocode for the ICAN scheme. The deep autoencoder network receives absorption coefficients corresponding to 0 - 700 Hz as input and returns the geometric features as the output.

abstract form is these four geometric parameters. Notably, this inverse identification of attributes is performed in a supervised manner. A total of 500 epochs is performed to train and validate and the losses of ICAN model is estimated and is shown in Fig. 6b. The train and validation errors are significantly decreased up to 300 epochs, after that the losses converged to a minimal value. Following the successful training on the HIRCN dataset, the new model is evaluated on a mutually exclusive test-set of 15000 samples.

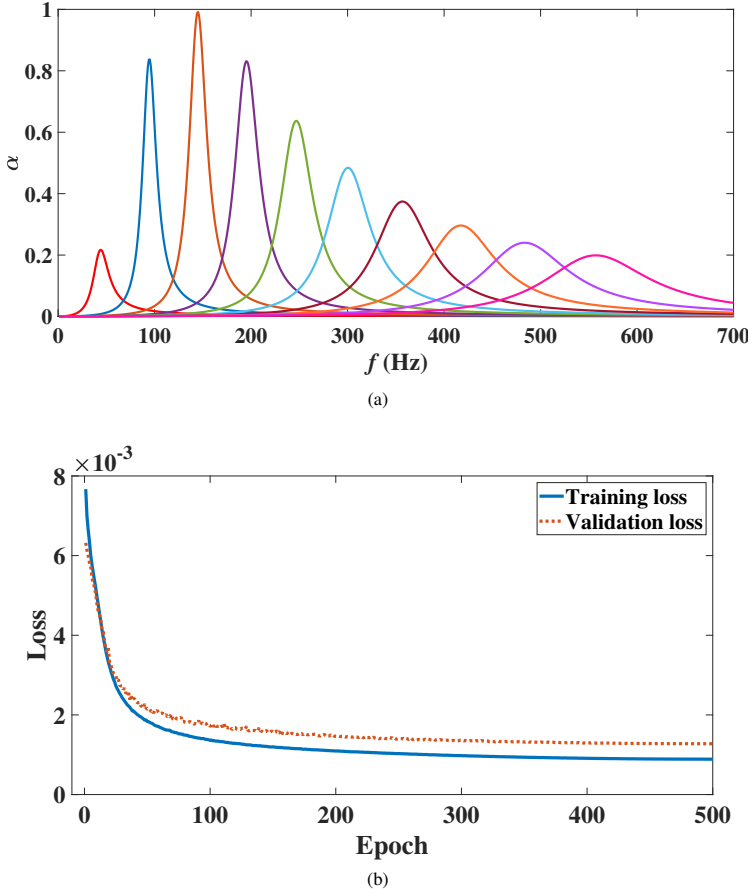


Fig. 6: (a) A representative dataset of absorption spectra for HRICN configuration obtained through analytical methodology (refer Eq. 27) (b) The training and validation losses of the ICAN model for 500 epochs on the HRICN dataset.

A set of 1000 samples are randomly picked from this test data and the predicted geometrical attributes of the absorber are marked in parity plots as shown in Fig. 7a-d. Here, the estimated and the true values of the geometric parameters are demarcated along with the diagonal line indicating exact correlation. It is evident that, the ICAN showed excellent prediction accuracy for all the four features. Finally, a comparative analysis of ICAN method with an established IDDN technique is performed. In fact, the IDDN scheme is efficient in dealing with inverse problems [29] and the implementation details are available in Appendix B. However, in the case of IDDN, the predicted and true values of geometric parameters are not in good accord, especially for l_N and r_C the discrepancy is higher which is also evident in the parity plots shown in Fig. 7e-h. These results demonstrated the prediction supremacy of ICAN over IDDN. To corroborate this, root mean square error (RMSE) is determined for

Table 3: Comparison of RMSE between predicted and true values of r_N , l_N , r_C and l_C which are inversely predicted from 1000 random samples drawn from the HRICN test dataset. The predictions are done using ICAN and IDDN schemes.

Geometrical parameter	RMSE between predicted and true value (mm)	
	IDDN	ICAN
l_N	18.79	9.19
r_N	0.65	0.48
l_C	7.25	4.79
r_C	6.01	2.90

the geometrical parameters by IDDN and ICAN as per the relation,

$$\text{RMSE} = \sqrt{\frac{1}{n} \sum_{i=1}^n (y_i - \hat{y}_i)^2}. \quad (16)$$

The RMSE values of predicted geometrical parameters by IDDN and ICAN method is given in Table 3 and are also provided in Fig. 7. These RMSE values also emphasize that ICAN is a better model than IDDN. In other words, autoencoder performs better than conventional DNN in the case of inverse prediction.

A major shortcoming of IDDN method is that, it requires a priori information on at least one of the geometrical attribute of the absorber in addition to the input frequency-response. Such prior information is required for IDDN to solve the issue of non-unique solutions. From the previous research work [29], it was observed that IDDN has a poor performance, when prior information about the geometry is unavailable. Multiple and inaccurate predictions were done by IDDN, when input data was fed without any previous knowledge on the absorber geometry. In contrast, ICAN needs only the absorption spectrum as input. In fact, the requirement of a priori information on some geometrical features of the acoustic-absorber limits the application of the traditional IDDN. Often, IDDN performs well, if a pre-determined geometrical attribute is supplied to the inverse algorithm whereas it gives erroneous results when previous knowledge about the absorber geometry is unavailable [29]. To cross verify this, a comparison of ICAN and IDDN schemes is carried out for HRICN geometry. For this, IDDN schemes with and without prior information are modelled to inversely design an HRICN. At first, the cavity radius (r_C), which is the least influencing parameter [29, 78], is prefixed and is given as an additional input along with absorption spectrum to IDDN. The remaining geometrical features are inversely forecasted by IDDN and the corresponding absorption characteristics obtained is plotted along with experimental data in Fig. 8a. Next, the IDDN is executed separately without any pre-determined geometrical feature and absorption response is plotted in Fig. 8a. Note that, within the frequency range of 100–300 Hz, the absorption coefficients predicted by IDDN shows an average variation of 19%, which is more than that of the IDDN with r_C given a priori (4%). It is evident that, IDDN cannot be trusted for the inverse design, if prior information on absorber geometry is unobtainable.

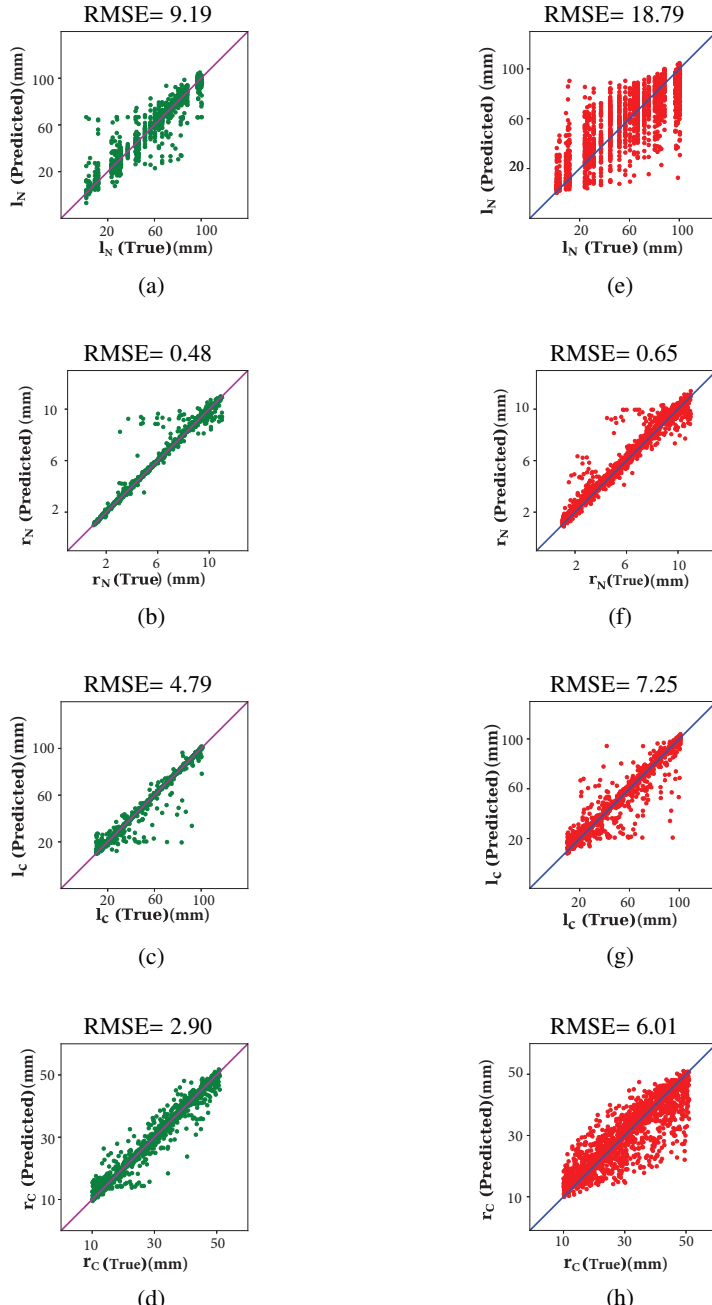


Fig. 7: Comparison of predicted and true values of r_N , l_N , r_C , and l_C , which are inversely predicted from 1000 random samples drawn from the HRICN test dataset. The predictions are done using ICAN [(a)-(d)] and IDDN [(e)-(h)] schemes. The diagonal line represents the ideal correlation.

Table 4: Estimated and actual geometric parameters of HRICN. For both IDDN and ICAN absorption coefficients (α) corresponding to the frequencies of 0 - 700 Hz is given as input.

Parameters	Actual value (mm) [20]	ICAN		IDDN		IDDN - prefixed r_C	
		Predicted value (mm)	Relative error (%)	Predicted value (mm)	Relative error (%)	Predicted value (mm)	Relative error (%)
l_N	80	83.2	4	73.9	7.62	82.81	3.5
r_N	2.2	2.24	1.8	1.84	16.36	2.24	1.8
l_C	50	50.6	1.2	43.06	13.88	51.5	3
r_C	13.3	13.17	0.97	14.18	6.6	—	—

To provide an independent evaluation, the absorption spectrum of HRICN from previous literature [20], is fed into the ICAN and the geometric parameters of HRICN are inversely speculated as shown in Table 4. Importantly, the maximum error in forecast is noted for the parameter l_N and that is only 4%, which indeed underscore the fidelity of ICAN scheme. Subsequently, using the four predicted geometric attributes of HRICN, the absorption coefficients are analytically estimated (Eq. 27) and compared with the experimental results [20] as shown in Fig. 8b. Moreover, the predicted absorption characteristics shown close agreement with experimental results, with an average error of 3.5%, which is significantly lower than the traditional IDDN scheme. It is noteworthy that, the maximum deviation observed in predicting one of the four parameters (r_N) using IDDN is around 16%, while that by ICAN is 4%. Thereby, it is evident that ICAN outperforms IDDN in terms of prediction capabilities.

In order to compare the prediction capability of IDDN against ICAN, their performance on the same dataset is tested. For this, IDDN is trained and tested with HRICN dataset having absorption characteristics from 0 to 700 Hz as the input and four geometric parameters as the output. The loss curves from both schemes on validation set are determined computationally. For this, the mean absolute error (MAE) and mean absolute percentage error (MAPE) are chosen as metrics. They are defined as,

$$\text{MAE} = \frac{1}{n} \sum_{i=1}^n |y_i - \hat{y}_i|, \quad (17)$$

and

$$\text{MAPE} = \frac{100}{n} \sum_{i=1}^n \left| \frac{y_i - \hat{y}_i}{y_i} \right| \%. \quad (18)$$

The MAE and MAPE loss history of ICAN and IDDN models based on the predicted geometric attributes of the validation sets are given in Fig. 9. In the ICAN model, geometric parameters are obtained as encoder output, in contrast, the IDDN model generates geometric features in the final dense layer. After 500 epochs of training on HRICN dataset, the MAPE and MAE metrics of IDDN are approximately 20% and 0.004 respectively, whereas the MAPE loss of ICAN reduces to about 7% and MAE reduces to 9.1×10^{-4} . Thus, MAPE loss of ICAN is approximately 13% lower

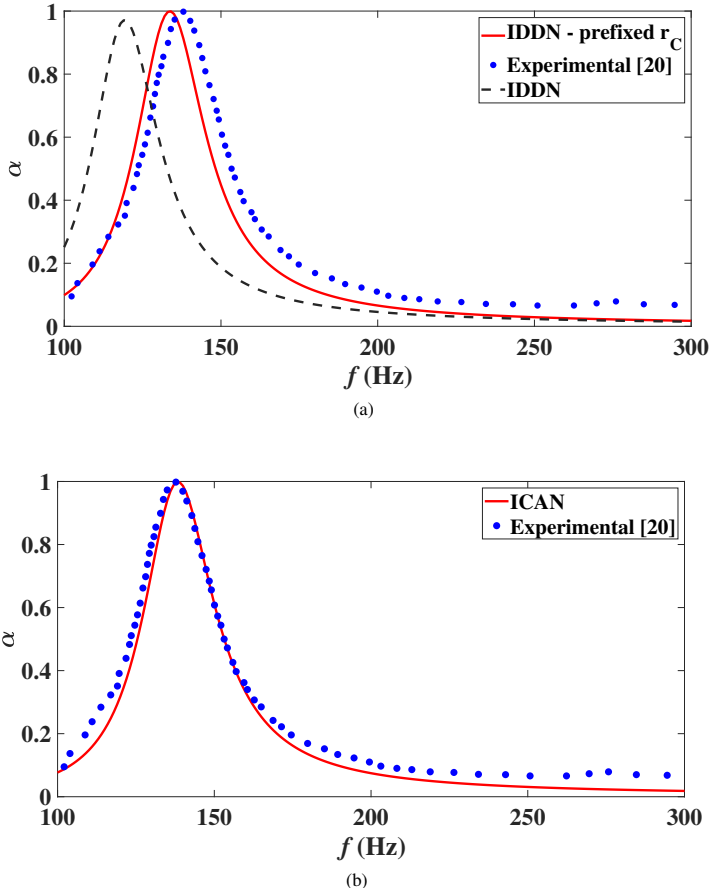


Fig. 8: (a) Comparison of sound absorption characteristics of HRICN absorbers with the geometric features predicted by IDDN and IDDN with prefixed r_C and experimental observations of Huang et al. [20]. (b) Comparison of sound absorption characteristics of HRICN absorber with the geometric features predicted by ICAN and experimental observations by Huang et al. [20].

than that of IDDN. Moreover, on comparing the computational load, IDDN needs 23 million parameters to map the relation between absorption characteristics and geometric parameters while ICAN needed only 7.3 million parameters for the inverse mapping. ICAN is thus less computational intensive than IDDN. Hence, ICAN is expected to be more competitive in dealing with complicated absorber geometries that demands further in-depth assessment.

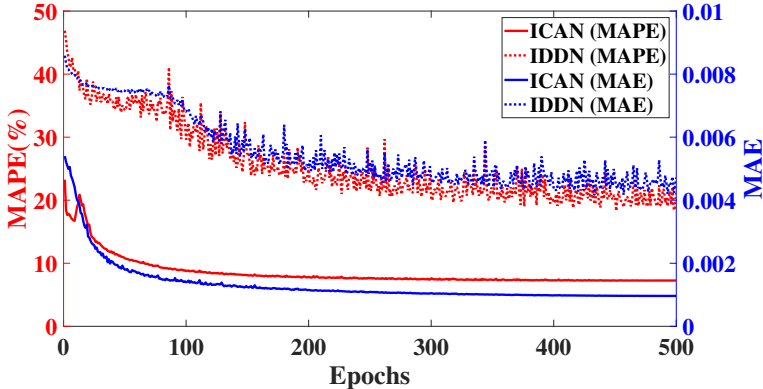


Fig. 9: The validation losses of ICAN and IDDN models, where the left axis shows MAPE loss and right axis shows MAE loss. The losses are based on the prediction of geometrical parameters of HRICN.

4 Inverse design of composite MHRICN absorber

The MHRICN configuration is found to be very effective for the mitigation of broadband low-frequency noise (see Sec. 2). The proposed ICAN scheme is extended to geometrically complex MHRICN absorber to maximize their absorption capabilities in selected frequency ranges. The MHRICN configuration is a parallel arrangement of four HRICNs and a circular MPP (see Fig. 1a). Using the ICAN scheme, the geometric parameters of these four HRICNs and MPP is inversely estimated. To provide maximum flexibility in the design process, a total of 11 model attributes are selected for inverse prediction. Selected attributes include eight geometric parameters (neck radii (r_{Ni}) and neck lengths (l_{Ni})) of four HRICNs and the three design parameters of MPP such as diameter of hole (d), panel thickness (t) and porosity (σ).

Using the analytical methodology (refer Sec. 2.2), absorption characteristics are obtained for different combinations of the eleven geometric attributes. Here also, the frequency regime considered for data generation is 0 - 700 Hz. During data preparation, using Eq. 6, the backing cavity length of MPP (l_p) and diameter of MHRICN (D) are kept constant as 70 mm and 100 mm respectively. At the same time, the cavity length (l_C) and cavity radius (r_C) of all HRICNs are fixed as 50 mm and 15 mm respectively. The remaining 11 geometric dimensions chosen for data preparation are given in Table 5. Among them, the neck lengths and neck radii are chosen according to the frequency of interest. Meanwhile, the data range of MPP are chosen to consider their broad absorption characteristics in the selected frequency range. The chosen dimensions of MPP are capable to accomplish broad band absorption up to a low frequency limit of 200 Hz. To further shift their absorption to lower frequencies, longer backing cavity length is necessary, which inevitably increase the thickness of the absorber. However, using the selected dimensions a vast dataset consisting of 314928 data samples are produced. A randomly created sample dataset which represent absorption spectra over the entire 0 - 700 Hz frequency regime is shown in

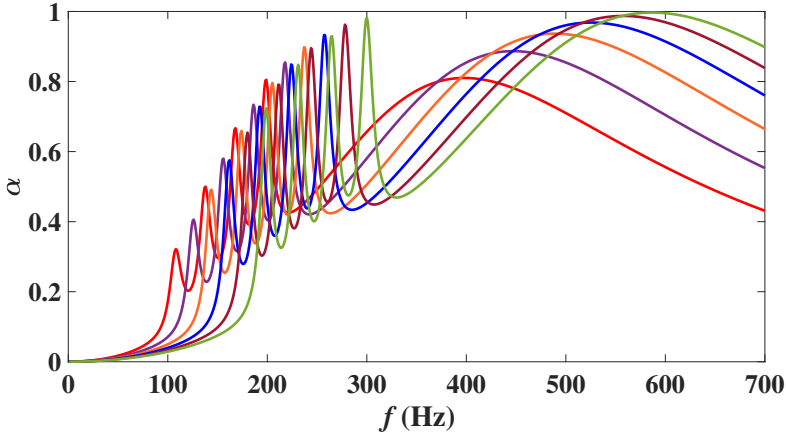


Fig. 10: A representative dataset of absorption spectra of MHRICN configuration obtained through analytical methodology (refer Eq. 6).

Table 5: The dimensions selected for data production in order to forecast geometrical features of MHRICN. The parameters kept as fixed are $l_p = 70$ mm, $D = 100$ mm, $r_C = 15$ mm and $l_C = 50$ mm.

Parameters	Limit of random values
$(l_{Ni})_{i=1,2,3,4}$	60-120 mm
$(r_{Ni})_{i=1,2,3,4}$	3-6 mm
d	0.2-2 mm
σ	0.5 % to 3 %
t	1-3 mm

Fig. 10. From the generated dataset, data bins of 236197, 47239 and 31492 samples are categorized as train, validation and test respectively. The chance of defective data sample in each set is totally eliminated by thorough cross-checking.

Here, ICAN is used to map the relation between absorption coefficients and 11 geometric parameters of MHRICN. As the output of the encoder is the estimated 11 geometric parameters, the intermediate dense layer has 11 neurons. All other layer features are the same as that of Table 1. For training and testing of all hyperparameters, loss function and optimizer are chosen as same as that of HRICN (refer Sec. 3.2). The ICAN takes the one-dimensional array of 700 absorption coefficients as input and predicts geometric parameters as encoder output, while the decoder returns estimated absorption coefficients. This ICAN scheme is successfully trained using the train dataset. A set of 1000 samples are randomly picked from the test set and they are marked in parity plots as depicted in Fig. 11a-k. The respective RMSE estimation between predicted and true values is given in Table 6 and specified in Fig. 11. The estimated and true values of all geometric parameters are in good accord. Hence, ICAN is demonstrated to be effective, in the inverse design of MHRICN. Finally, the ICAN technique is extended to forecast the design parameters of various

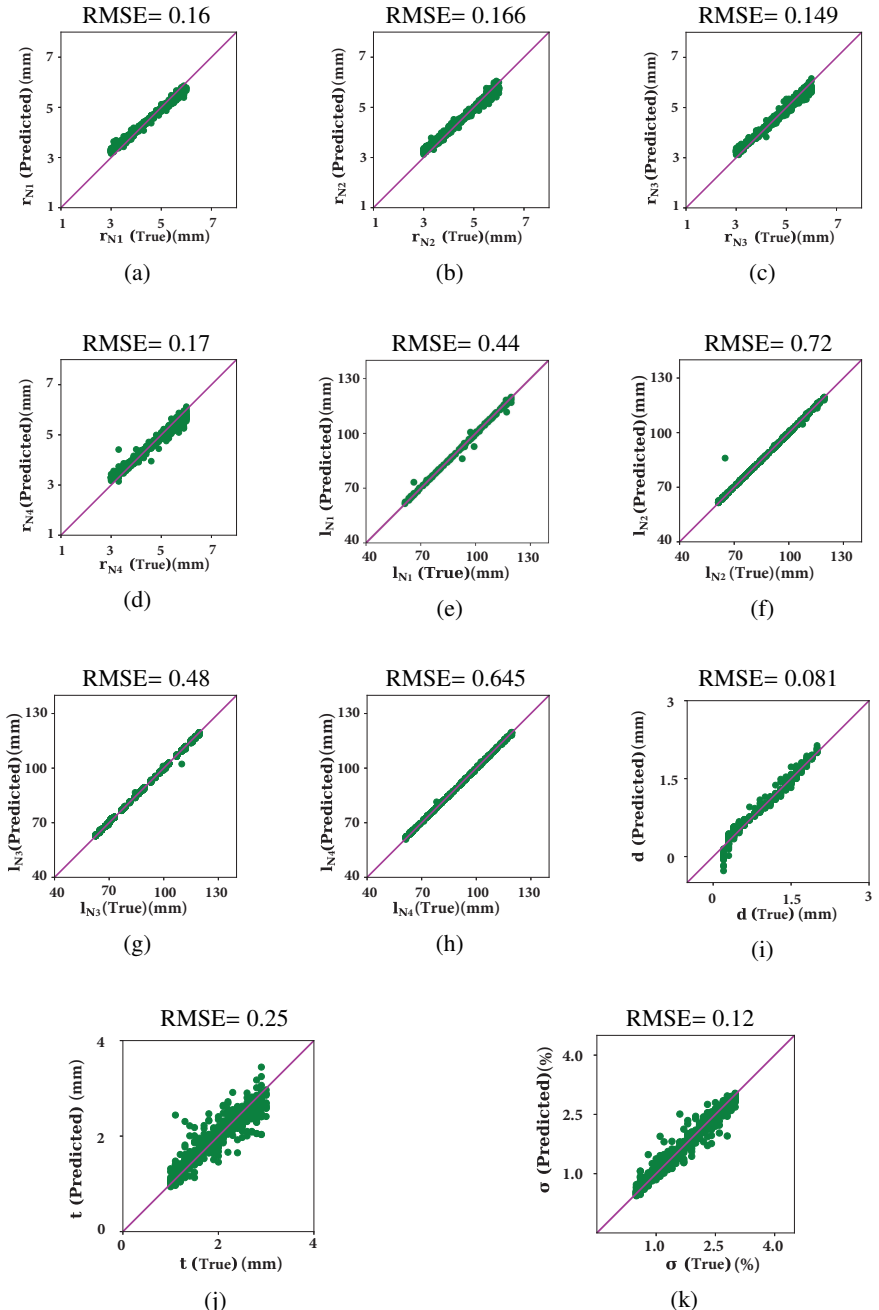
A deep autoencoder based approach for the inverse design of an acoustic-absorber

Fig. 11: Comparison of predicted and true values of r_{Ni} [(a)-(d)], l_{Ni} [(e)-(h)], d , t and σ [(i)-(k)] of thousand random samples drawn from the MHRICN test dataset. The diagonal line represents the perfect correlation between the estimated and true data.

Table 6: RMSE between predicted and true values of r_{Ni} , l_{Ni} , d , t and σ , which are inversely predicted from 1000 random samples drawn from the MHRICN test dataset. The predictions are done using the ICAN scheme.

Geometrical feature	RMSE between predicted and true value
r_{N1}	0.16
r_{N2}	0.166
r_{N3}	0.149
r_{N4}	0.17
l_{N1}	0.44
l_{N2}	0.72
l_{N3}	0.48
l_{N4}	0.645
d	0.081
t	0.25
σ	0.12

MHRICN configurations with specific functionality. Note that ICAN does not produce a feasible result for an unrealistic absorption spectrum. Typically, an MHRICN absorber with four inhomogeneous HRs produces four narrowband peaks and one broadband peak. For illustration, four entirely different absorption spectra (A1-A4) are selected randomly and fed through ICAN to predict the design parameters. In all the four instances, the ICAN generates plausible outputs corresponding to the respective absorption spectra, and the estimated parameters are listed in Table 7. The absorption responses are reconstructed using absorbers with predicted design parameters and compared with the target spectra as illustrated in Fig. 12a-d. The red solid lines represent the estimated spectra (Eq. 6) and the blue dotted lines represent the desired spectra. The discrepancy between predicted and desired absorption spectra is depicted in Fig. 12e-h. It shows that, the error is very low in all absorber configurations. The prediction errors are mostly accumulated on peak frequencies, with A2 and A3 exhibiting relatively higher prediction errors than A1 and A4.

In the low and mid-frequency domains, all of these absorber types exhibit remarkable absorption properties. Especially, configurations A2, A3 and A4 exhibit 85% sound absorption over a bandwidth of two one-third octave-bands. Meanwhile, configuration A1 has a sound absorption rate of 80% throughout the frequency range of 200-315 Hz. It is worth noting that only four absorption peaks are visible in the obtained spectra of the A1 configuration, see Fig. 12a. Note that, for A1 configuration resonance frequencies of two HRICNs (f_1 & f_2) are exactly the same. Moreover, all of these designs have a maximum thickness of 7.3 cm only. Further, the sound absorption characteristics and thickness of the proposed absorber is compared with that available in the literature and is given in Table 8. Most of them have a greater thickness or have low absorption levels in the frequency range less than 300 Hz. Even though hybrid absorbers like combination of parallel-arranged MPP and Archimedean-inspired spiral (AIS) absorber [27] and the absorber based on microporforated panel and coiled-up channels [26] have comparatively lower thickness, their absorption effectiveness below 300 Hz is quite poor. Moreover, their mechanical structure is highly complex. Meanwhile, the absorber composed of parallel arranged

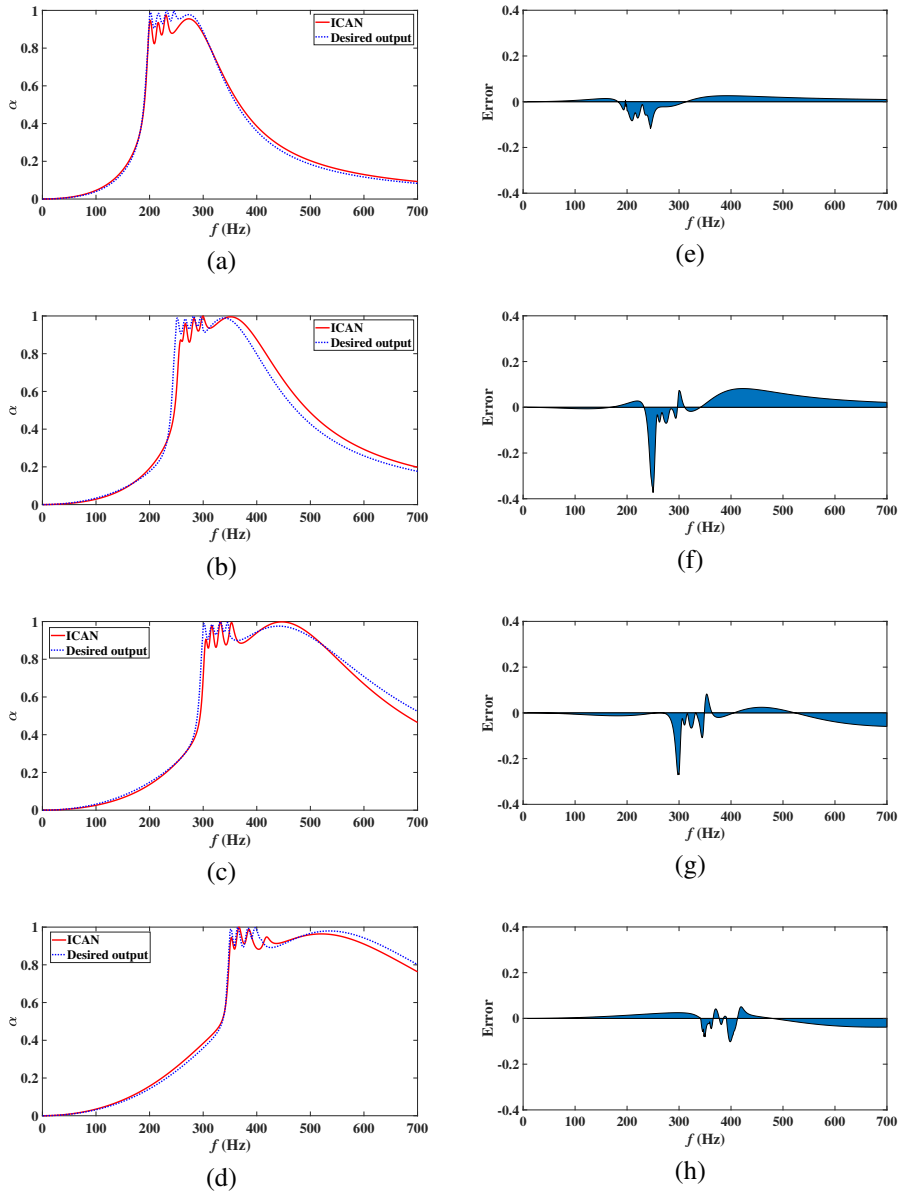
A deep autoencoder based approach for the inverse design of an acoustic-absorber

Fig. 12: Comparison of the required absorption characteristics with the absorption characteristics obtained by the ICAN method for MHRICN models (a) A1, (b) A2, (c) A3, and (d) A4. [(e)–(h)] The variation between predicted and obtained spectra of the corresponding models A1 - A4.

Table 7: Predicted design parameters of MHRICN absorbers (A1-A4). For all absorbers, $l_{Ci} = 50$ mm, $r_{Ci} = 15$ mm, $D = 100$ mm and $l_p = 70$ mm. f_1, f_2, f_3 and f_4 are the resonance frequencies of HRICNs and f_5 is the resonance frequency of MPP.

Absorption Characteristics	Predicted design parameters of HRICNs and MPP	Resonance frequencies (Hz)	Variation between the desired and obtained spectra (%)
(A1) 80% absorption in the frequency regime of 200-315 Hz	$l_{N1}=91$ mm, $r_{N1}=3.65$ mm, $l_{N2}=112.3$ mm, $r_{N2}=3.9$ mm, $l_{N3}=93.6$ mm, $r_{N3}=4.15$ mm, $l_{N4}=92.1$ mm, $r_{N4}=3.9$ mm, $d=0.9$ mm, $t=2.9$ mm, $\sigma=0.8\%$	$f_1=201,$ $f_2=201,$ $f_3=216,$ $f_4=231,$ $f_5=273$	1.77
(A2) 85% absorption in the frequency regime of 255-400 Hz	$l_{N1}=69.2$ mm, $r_{N1}=4.1$ mm, $l_{N2}=112$ mm, $r_{N2}=4.9$ mm, $l_{N3}=71.1$ mm, $r_{N3}=4.5$ mm, $l_{N4}=99.5$ mm, $r_{N4}=5.2$ mm, $d=0.8$ mm, $t=2.5$ mm, $\sigma=1.2\%$	$f_1=258,$ $f_2=267,$ $f_3=283,$ $f_4=299,$ $f_5=351$	3.68
(A3) 85% absorption in the frequency regime of 300-530 Hz	$l_{N1}=102.3$ mm, $r_{N1}=5.3$ mm, $l_{N2}=114.3$ mm, $r_{N2}=5.55$ mm, $l_{N3}=103.6$ mm, $r_{N3}=5.65$ mm, $l_{N4}=98.7$ mm, $r_{N4}=5.85$ mm, $d=0.6$ mm, $t=2.1$ mm, $\sigma=1.7\%$	$f_1=305,$ $f_2=316,$ $f_3=332,$ $f_4=353,$ $f_5=447$	2.37
(A4) 85% absorption in the frequency regime of 350-650 Hz	$l_{N1}=75.3$ mm, $r_{N1}=5.5$ mm, $l_{N2}=71.7$ mm, $r_{N2}=5.6$ mm, $l_{N3}=98.6$ mm, $r_{N3}=6.2$ mm, $l_{N4}=75.9$ mm, $r_{N4}=6.3$ mm, $d=0.4$ mm, $t=1.6$ mm, $\sigma=1.9\%$	$f_1=353,$ $f_2=367,$ $f_3=385,$ $f_4=418,$ $f_5=520$	1.92

perforated plates with extended tubes and porous material [79] has higher thickness and its absorption capacity is lower. Indeed, the proposed A1 configuration exhibits 80% absorption in the frequency regime of 200-315 Hz with a sub-wavelength thickness of 7.2 cm ($\lambda/23$ at 200 Hz). Moreover, the absorption bandwidths of A1-A4 cover the whole frequency range of 200 - 700 Hz. To further expand the bandwidth of absorption to lower frequencies, longer backing cavities can be employed. The proposed sound absorber system is compact, robust, and effortless to fabricate. Hence, the proposed absorber designs may be easily produced by employing additive manufacturing techniques such as stereo-lithography, fused deposition modelling, or selective laser sintering. Most importantly, this novel inverse design technique based on convolutional autoencoders is found to be highly successful in the construction of complicated sound absorbers such as MHRICNs with great precision and fidelity. In addition, the ICAN techniques may be easily extended to the inverse design of complex acoustic structures such as acoustic cloaks, split-ring resonators, membrane type metamaterials, Fabry-Perot absorbers, and so on. To improve the efficiency of this scheme, future studies have to be focused on physics-informed neural networks.

5 Conclusions

In this study, a novel low frequency acoustic-absorber configuration consisting of MPP and multiple HRICNs is presented. A convolutional autoencoder-based deep neural network is developed for the inverse speculation of geometrical features of

Table 8: Comparison of sound absorption characteristics and thickness of MHRICN absorber with that available in the literature.

Model details	Absorption characteristics	Thickness (cm)
Microperforated panel absorber backed by Helmholtz resonator (Park [25])	Two narrow band peaks of 90 % absorption at 100 Hz and 630 Hz.	17
Parallel-arranged MPP and Archimedean-inspired spiral (AIS) absorber (Boccaccio et al. [27])	60% absorption in the frequency regime of 380 Hz to 1250 Hz	2.43
Hybrid absorber based on microperforated panel and coiled-up channels (Wu et al. [26])	90% absorption in the frequency regime of 350 Hz to 470 Hz	5
Parallel arranged perforated plates with extended tubes and porous material (Li et al. [79])	60% absorption in the frequency regime of 180 Hz to 350 Hz	10.5
Multi-layer Helmholtz resonators with extended necks (Guo et al. [80])	80% absorption in the frequency regime of 300 Hz to 550 Hz	6.1
Multilayer microperforated panel absorber (Bucciarelli et al. [81])	85% absorption in the frequency regime of 400 Hz to 2000 Hz	14.3
Parallel combination of MPP with Helmholtz resonator with inserted neck (Mahesh et al. [29])	65% absorption in the frequency regime of 200 to 250 Hz.	7.2
MHRICN model A1 (present study)	80% absorption in the frequency regime of 200 Hz to 315 Hz	7.3

acoustic-absorbers. The new ICAN technique is successfully applied on an existing simple HRICN absorber and is extended later to a complex MHRICN. The major findings of the study are enlisted below.

- The introduced low-frequency acoustic-absorber, MHRICN, is compact and exhibited remarkable absorption characteristics over a broadband of frequencies.
- A mathematical model based on electro-acoustic theory is formulated for MHRICN to create the large dataset required to train the deep neural network.
- Autoencoder based inverse design technique ICAN, is developed for complex acoustic-absorbers and is successfully tested on MHRICN. The geometrical attributes estimated by the ICAN differed from the true values by less than 4%.
- In terms of prediction accuracy and computational load, the ICAN outperformed the traditional IDDN. For the same test case, IDDN yielded an error value of 16.4%, whereas ICAN produced only 4%.
- The learnable parameters required for the IDDN to inversely map the relation between absorption characteristics and geometric parameters are 23 million, whereas for ICAN it is only 7.3 million. Since, the learnable parameters involved are very less, the ICAN is quicker and efficient in inverse predictions.
- Since, ICAN requires no pre-design information of geometrical features, it offers more effective solution for inverse design problems in comparison with traditional IDDN.

- The design parameters of four distinct MHRICN models are forecasted using ICAN method and these models exhibited quasi-perfect absorption in the frequency bands of 200-315 Hz, 255-400 Hz, 300-530 Hz and 350-650 Hz.

In a nutshell, the exceptional broadband low-frequency absorption characteristics and compact size of the suggested MHRICN absorber make it suitable for low-frequency noise mitigation applications such the acoustic protection systems of payload fairing, noise reduction in automotive, aeroplane fuselages, HVAC, interior rooms, and so on.

Acknowledgements

One of the authors (K. Mahesh) gratefully acknowledges the research sponsorship under the AICTE Doctoral Fellowship (Government of India) scheme. The authors also acknowledge the funding obtained under FIST-DST scheme (SR/FST/384) to carry out the current research work.

Declarations

Conflict of interest

The authors have no conflicts of interest to declare that are relevant to the content of this article.

Appendices

A Theoretical model of HRICN

The equivalent medium theory [82] is used to analyze the absorption characteristics of the HRICN. With this theory, the acoustic characteristics of neck and cavity of HRICN are separately modelled. Thus, when considering the visco-thermal losses, the complex density ($\rho_{N,C}^c$), complex wave number ($k_{N,C}^c$) and complex sound speed ($c_{N,C}^c$) of fluid propagating through the neck and cavity are formulated as [82, 83],

$$k_{N,C}^c = k \sqrt{\frac{\gamma - (\gamma - 1)\psi_{N,C}^h}{\psi_{N,C}^v}}, \quad (19)$$

$$\rho_{N,C}^c = \frac{\rho}{\psi_{N,C}^v}, \quad (20)$$

and

$$c_{N,C}^c = \frac{\omega}{k_{N,C}^c}, \quad (21)$$

where k is the wave number and γ is the specific heat ratio of air. Further, $\psi_{N,C}^v$ and $\psi_{N,C}^h$ are the functions of viscous and thermal fields inside the neck and cavity, which

A deep autoencoder based approach for the inverse design of an acoustic-absorber

are formulated as [82, 83],

$$\psi_{N,C}^v = -\frac{J_2(k_v d_{N,C}/2)}{J_0(k_v d_{N,C}/2)}, \quad (22)$$

$$\psi_{N,C}^h = -\frac{J_2(k_h d_{N,C}/2)}{J_0(k_h d_{N,C}/2)}, \quad (23)$$

where $k_v = \sqrt{-j\frac{\omega\rho}{\eta}}$ is the viscous wavenumber and $k_h = \sqrt{-j\frac{\omega\rho c_p}{K}}$ is the thermal wavenumber. J_2 and J_0 are the Bessel functions of first kind and order two and zero respectively.

Using Eqns.(19)-(23), the acoustic impedance of neck (Z_N) is formulated as,

$$Z_N = j \frac{2\rho c \sin(k_N^c l_N/2)}{\sqrt{(\gamma - (\gamma - 1)\psi_N^h)\psi_N^v}}, \quad (24)$$

Due to the insertion of the neck into the cavity, the cavity has an irregular shape. Hence, its acoustic impedance is represented using its effective volume. The effective volume of the cavity $V = \pi r_C^2 l_C - \pi r_N^2 l_N$, where $r_N = d_N/2$ and $r_C = d_C/2$ are the neck and the cavity radii, respectively. Thereby, the acoustic impedance of the cavity is given by,

$$Z_V = -j \frac{S_N \rho_C^c (c_C^c)^2}{\omega V}. \quad (25)$$

From Z_N and Z_V the total acoustic impedance of HRICN is evaluated as,

$$Z_{HR} = \frac{A}{S_N} \left(Z_N + Z_V + 2\sqrt{2\omega\rho\eta} + j\omega\rho\delta \right), \quad (26)$$

where $A = \pi r_C^2$ is the cross-sectional area of the HRICN and $S_N = \pi r_N^2$ is the cross-sectional area of the inserted curvy neck. In addition, $\delta = (1 + (1 - 1.25\varepsilon))(4/3\pi)d_N$ is the end correction length of inserted neck, in which $\varepsilon = \frac{d_N}{d_C}$ is the ratio of diameter of the neck to diameter of the cavity. Finally, the frictional resistance ($2\sqrt{2\omega\rho\eta}$) offered by the inner boundaries of the inserted neck is also added to the acoustic resistance. From Z_{HR} , the absorption coefficient of HRICN is obtained as,

$$\alpha = 1 - \left| \frac{Z_{HR} - z_0}{Z_{HR} + z_0} \right|^2. \quad (27)$$

B Inverse design using deep neural network(IDDN)

For the comparative analysis of IDDN and ICAN schemes, the IDDN scheme is applied to the HRICN absorber to forecast the four geometrical parameters such as l_N , r_N , l_C , and r_C . The absorption coefficients corresponding to 0 - 700 Hz are given

Table 9: The details of the IDDN model used for the comparative study. Linear activation is used for output layer, whereas rectified linear activation function (ReLU) is used for all other layers.

No	Layer Type	Layer Details	Output Shape	Parameters
1	Conv 1D	64×10, Strides=1, Input shape = (700, 1)	691×64	704
2	Conv 1D	32×10, Strides=1	682×32	20512
3	Flatten	-	21824	0
4	Dense	1024	1024	22348800
5	Dense	512	512	524800
6	Dense	256	256	131328
7	Dense	128	128	32896
8	Dense	64	64	8256
9	Dense	32	32	2080
10	Dense	4	4	132

as the input and the IDDN predicts the respective geometric parameters. The details of the IDDN architecture is given in Table 9. For training and testing, mean absolute error loss function is used. The datasets and hyperparameters for both the IDDN and ICAN schemes are same. More details on the implementation are available in the previous work [29].

References

- [1] Babisch, W., Ising, H., Gallacher, J.: Health status as a potential effect modifier of the relation between noise annoyance and incidence of ischaemic heart disease. *Occupational and Environmental Medicine* **60**(10), 739–745 (2003)
- [2] Dratva, J., Phuleria, H.C., Foraster, M., Gaspoz, J.-M., Keidel, D., Künzli, N., Liu, L.-J.S., Pons, M., Zemp, E., Gerbase, M.W., *et al.*: Transportation noise and blood pressure in a population-based sample of adults. *Environmental Health Perspectives* **120**(1), 50–55 (2012)
- [3] Muzet, A.: Environmental noise, sleep and health. *Sleep Medicine Reviews* **11**(2), 135–142 (2007)
- [4] Miedema, H., Oudshoorn, C.: Annoyance from transportation noise: relationships with exposure metrics dnl and denl and their confidence intervals. *Environmental Health Perspectives* **109**(4), 409–416 (2001)
- [5] Licita, G., Fredianelli, L., Petri, D., Vigotti, M.A.: Annoyance evaluation due to overall railway noise and vibration in Pisa urban areas. *Science of the Total Environment* **568**, 1315–1325 (2016)
- [6] Tang, X., Yan, X.: Acoustic energy absorption properties of fibrous materials: A review. *Composites Part A: Applied Science and Manufacturing* **101**, 360–380 (2017)

- [7] Cao, L., Fu, Q., Si, Y., Ding, B., Yu, J.: Porous materials for sound absorption. *Composites Communications* **10**, 25–35 (2018)
- [8] Ingard, U.: On the theory and design of acoustic resonators. *The Journal of the Acoustical Society of America* **25**(6), 1037–61 (1953)
- [9] Prydz, R., Wirt, L., Kuntz, H., Pope, L.: Transmission loss of a multilayer panel with internal tuned Helmholtz resonators. *The Journal of the Acoustical Society of America* **87**(4), 1597–1602 (1990)
- [10] Kim, S., Kim, Y.H., Jang, J.H.: A theoretical model to predict the low-frequency sound absorption of a Helmholtz resonator array. *The Journal of the Acoustical Society of America* **119**(4), 1933–1936 (2006)
- [11] Mahesh, K., Mini, R.S.: Investigation on the acoustic performance of multiple Helmholtz resonator configurations. *Acoustics Australia*, 1–15 (2021)
- [12] Cambonie, T., Mbailassem, F., Gourdon, E.: Bending a quarter wavelength resonator: Curvature effects on sound absorption properties. *Applied Acoustics* **131**, 87–102 (2018)
- [13] Cambonie, T., Gourdon, E.: Innovative origami-based solutions for enhanced quarter-wavelength resonators. *Journal of Sound and Vibration* **434**, 379–403 (2018)
- [14] Maa, D.-Y.: Theory and design of microperforated panel sound-absorbing constructions. *Scientia Sinica* **18**(1), 55–71 (1975)
- [15] Maa, D.-Y.: Microperforated-panel wideband absorbers. *Noise Control Engineering Journal* **29**(3), 77 (1987)
- [16] Maa, D.-Y.: Potential of microperforated panel absorber. *The Journal of the Acoustical Society of America* **104**(5), 2861–2866 (1998)
- [17] Wang, C., Cheng, L., Pan, J., Yu, G.: Sound absorption of a micro-perforated panel backed by an irregular-shaped cavity. *The Journal of the Acoustical Society of America* **127**(1), 238–246 (2010)
- [18] Wang, C., Huang, L.: On the acoustic properties of parallel arrangement of multiple micro-perforated panel absorbers with different cavity depths. *The Journal of the Acoustical Society of America* **130**(1), 208–218 (2011)
- [19] Li, X., Wu, Q., Kang, L., Liu, B.: Design of multiple parallel-arranged perforated panel absorbers for low frequency sound absorption. *Materials* **12**(13), 2099 (2019)
- [20] Huang, S., Fang, X., Wang, X., Assouar, B., Cheng, Q., Li, Y.: Acoustic perfect absorbers via Helmholtz resonators with embedded apertures. *The Journal of*

the Acoustical Society of America **145**(1), 254–262 (2019)

- [21] Duan, M., Yu, C., Xu, Z., Xin, F., Lu, T.J.: Acoustic impedance regulation of Helmholtz resonators for perfect sound absorption via roughened embedded necks. *Applied Physics Letters* **117**(15), 151904 (2020)
- [22] Guo, J., Fang, Y., Jiang, Z., Zhang, X.: Acoustic characterizations of Helmholtz resonators with extended necks and their checkerboard combination for sound absorption. *Journal of Physics D: Applied Physics* **53**(50), 505504 (2020)
- [23] Guo, J., Zhang, X., Fang, Y., Jiang, Z.: A compact low-frequency sound-absorbing metasurface constructed by resonator with embedded spiral neck. *Applied Physics Letters* **117**(22), 221902 (2020)
- [24] Gai, X.L., Xing, T., Li, X.H., Zhang, B., Wang, F., Cai, Z.N., Han, Y.: Sound absorption of microperforated panel with L shape division cavity structure. *Applied Acoustics* **122**, 41–50 (2017)
- [25] Park, S.-H.: Acoustic properties of micro-perforated panel absorbers backed by Helmholtz resonators for the improvement of low-frequency sound absorption. *Journal of Sound and Vibration* **332**(20), 4895–4911 (2013)
- [26] Wu, F., Xiao, Y., Yu, D., Zhao, H., Wang, Y., Wen, J.: Low-frequency sound absorption of hybrid absorber based on micro-perforated panel and coiled-up channels. *Applied Physics Letters* **114**(15), 151901 (2019)
- [27] Boccaccio, M., Bucciarelli, F., Fierro, G.P.M., Meo, M.: Microperforated panel and deep subwavelength Archimedean-inspired spiral cavities for multi-tonal and broadband sound absorption. *Applied Acoustics* **176**, 107901 (2021)
- [28] Mahesh, K., Mini, R.S.: Theoretical investigation on the acoustic performance of Helmholtz resonator integrated microperforated panel absorber. *Applied Acoustics* **178**, 108012 (2021)
- [29] Mahesh, K., Kumar Ranjith, S., Mini, R.S.: Inverse design of a Helmholtz resonator based low-frequency acoustic absorber using deep neural network. *Journal of Applied Physics* **129**(17), 174901 (2021)
- [30] Tandis, E., Assareh, E.: Inverse design of airfoils via an intelligent hybrid optimization technique. *Engineering with Computers* **33**(3), 361–374 (2017)
- [31] Xu, H., Zhang, L., Li, Q.: A novel inverse procedure for load identification based on improved artificial tree algorithm. *Engineering with Computers*, 1–12 (2019)
- [32] Chen, P., Chen, C., Wang, H., Tsai, J., Ni, W.-X.: Synthesis design of artificial magnetic metamaterials using a genetic algorithm. *Optics Express* **16**(17),

- 12806–12818 (2008)
- [33] Sun, X., Jia, H., Yang, Y., Zhao, H., Bi, Y., Sun, Z., Yang, J.: Acoustic structure inverse design and optimization using deep learning. arXiv preprint arXiv:2102.02063 (2021)
 - [34] Goudos, S., Sahalos, J.: Microwave absorber optimal design using multi-objective particle swarm optimization. *Microwave and Optical Technology Letters* **48**(8), 1553–1558 (2006)
 - [35] Yoon, W.U., Park, J.H., Lee, J.S., Kim, Y.Y.: Topology optimization design for total sound absorption in porous media. *Computer Methods in Applied Mechanics and Engineering* **360**, 112723 (2020)
 - [36] Giannakoglou, K.C., Papadimitriou, D.I.: In: Thévenin, D., Janiga, G. (eds.) *Adjoint Methods for Shape Optimization*, pp. 79–108. Springer, Berlin, Heidelberg (2008)
 - [37] Peurifoy, J., Shen, Y., Jing, L., Yang, Y., Cano-Renteria, F., DeLacy, B.G., Joannopoulos, J.D., Tegmark, M., Soljačić, M.: Nanophotonic particle simulation and inverse design using artificial neural networks. *Science Advances* **4**(6), 4206 (2018)
 - [38] Chen, X., Wei, Z., Li, M., Rocca, P.: A review of deep learning approaches for inverse scattering problems (invited review). *Progress in Electromagnetics Research* **167**, 67–81 (2020)
 - [39] Hou, J., Lin, H., Xu, W., Tian, Y., Wang, Y., Shi, X., Deng, F., Chen, L.: Customized inverse design of metamaterial absorber based on target-driven deep learning method. *IEEE Access* **8**, 211849–211859 (2020)
 - [40] Harper, E.S., Coyle, E.J., Vernon, J.P., Mills, M.S.: Inverse design of broadband highly reflective metasurfaces using neural networks. *Physical Review B* **101**(19), 195104 (2020)
 - [41] Ma, J., Huang, Y., Pu, M., Xu, D., Luo, J., Guo, Y., Luo, X.: Inverse design of broadband metasurface absorber based on convolutional autoencoder network and inverse design network. *Journal of Physics D: Applied Physics* **53**(46), 464002 (2020)
 - [42] Gao, N., Wang, M., Cheng, B., Hou, H.: Inverse design and experimental verification of an acoustic sink based on machine learning. *Applied Acoustics* **180**, 108153 (2021)
 - [43] Balla, K., Sevilla, R., Hassan, O., Morgan, K.: An application of neural networks to the prediction of aerodynamic coefficients of aerofoils and wings. *Applied Mathematical Modelling* **96**, 456–479 (2021)

- [44] Shu, X., Bao, T., Li, Y., Gong, J., Zhang, K.: VAE-TALSTM: a temporal attention and variational autoencoder-based long short-term memory framework for dam displacement prediction. *Engineering with Computers*, 1–16 (2021)
- [45] Prayogo, D., Cheng, M.Y., Wu, Y.W., Tran, D.H.: Combining machine learning models via adaptive ensemble weighting for prediction of shear capacity of reinforced-concrete deep beams. *Engineering with Computers* **36**(3), 1135–1153 (2020)
- [46] Naser, M.: Can past failures help identify vulnerable bridges to extreme events? a biomimetical machine learning approach. *Engineering with Computers*, 1–33 (2019)
- [47] Liu, Z., Zhu, D., Rodrigues, S.P., Lee, K.-T., Cai, W.: Generative model for the inverse design of metasurfaces. *Nano Letters* **18**(10), 6570–6576 (2018)
- [48] Liu, D., Tan, Y., Khoram, E., Yu, Z.: Training deep neural networks for the inverse design of nanophotonic structures. *ACS Photonics* **5**(4), 1365–1369 (2018)
- [49] Tahersima, M.H., Kojima, K., Koike-Akino, T., Jha, D., Wang, B., Lin, C., Parsons, K.: Deep neural network inverse design of integrated photonic power splitters. *Scientific Reports* **9**(1), 1–9 (2019)
- [50] Sekar, V., Zhang, M., Shu, C., Khoo, B.C.: Inverse design of airfoil using a deep convolutional neural network. *AIAA Journal* **57**(3), 993–1003 (2019)
- [51] Han, X., Fan, Z., Liu, Z., Li, C., Guo, L.J.: Inverse design of metasurface optical filters using deep neural network with high degrees of freedom. *InfoMat* **3**(4), 432–442 (2021)
- [52] Kim, B., Lee, S., Kim, J.: Inverse design of porous materials using artificial neural networks. *Science Advances* **6**(1), 9324 (2020)
- [53] Iannace, G., Ciaburro, G., Trematerra, A.: Modelling sound absorption properties of broom fibers using artificial neural networks. *Applied Acoustics* **163**, 107239 (2020)
- [54] Jeon, J.H., Yang, S.S., Kang, Y.J.: Estimation of sound absorption coefficient of layered fibrous material using artificial neural networks. *Applied Acoustics* **169**, 107476 (2020)
- [55] Wang, Y., Yao, H., Zhao, S.: Auto-encoder based dimensionality reduction. *Neurocomputing* **184**, 232–242 (2016)
- [56] Geng, J., Fan, J., Wang, H., Ma, X., Li, B., Chen, F.: High-resolution SAR image classification via deep convolutional autoencoders. *IEEE Geoscience and*

Remote Sensing Letters **12**(11), 2351–2355 (2015)

- [57] An, J., Cho, S.: Variational autoencoder based anomaly detection using reconstruction probability. Special Lecture on IE **2**(1), 1–18 (2015)
- [58] Shu, X., Bao, T., Xu, R., Li, Y., Zhang, K.: Dam anomaly assessment based on sequential variational autoencoder and evidence theory. Applied Mathematical Modelling (2021)
- [59] Cheng, Y.: Semi-supervised learning for neural machine translation. In: Joint Training for Neural Machine Translation, pp. 25–40. Springer, Singapore (2019)
- [60] Bianco, M.J., Gerstoft, P., Traer, J., Ozanich, E., Roch, M.A., Gannot, S., Deledalle, C.-A.: Machine learning in acoustics: Theory and applications. The Journal of the Acoustical Society of America **146**(5), 3590–3628 (2019)
- [61] Hanakata, P.Z., Cubuk, E.D., Campbell, D.K., Park, H.S.: Forward and inverse design of kirigami via supervised autoencoder. Physical Review Research **2**(4), 042006 (2020)
- [62] Tang, Y., Kojima, K., Koike-Akino, T., Wang, Y., Wu, P., Xie, Y., Tahersima, M.H., Jha, D.K., Parsons, K., Qi, M.: Generative deep learning model for inverse design of integrated nanophotonic devices. Laser & Photonics Reviews **14**(12), 2000287 (2020)
- [63] Yonekura, K., Suzuki, K.: Data-driven design exploration method using conditional variational autoencoder for airfoil design. Structural and Multidisciplinary Optimization **64**(2), 613–624 (2021)
- [64] Jordan, J.: Introduction to autoencoders. Jeremy Jordan, Mar (2018)
- [65] Kiarashinejad, Y., Abdollahramezani, S., Adibi, A.: Deep learning approach based on dimensionality reduction for designing electromagnetic nanostructures. npj Computational Materials **6**(1), 1–12 (2020)
- [66] Ahmed, W.W., Farhat, M., Zhang, X., Wu, Y.: Deterministic and probabilistic deep learning models for inverse design of broadband acoustic cloak. arXiv preprint arXiv:2010.14866 (2020)
- [67] Congyun, Z., Qibai, H.: A method for calculating the absorption coefficient of a multi-layer absorbent using the electro-acoustic analogy. Applied Acoustics **66**(7), 879–887 (2005)
- [68] Munjal, M.L.: Acoustics of Ducts and Mufflers with Application to Exhaust and Ventilation System Design. John Wiley & Sons, Singapore (1987)

- [69] Tilmans, H.A.: Equivalent circuit representation of electromechanical transducers: I. lumped-parameter systems. *Journal of Micromechanics and Microengineering* **6**(1), 157 (1996)
- [70] Abbad, A., Atalla, N., Ouisse, M., Doutres, O.: Numerical and experimental investigations on the acoustic performances of membraned Helmholtz resonators embedded in a porous matrix. *Journal of Sound and Vibration* **459**, 114873 (2019)
- [71] Meng, H., Galland, M.-A., Ichchou, M., Bareille, O., Xin, F., Lu, T.: Small perforations in corrugated sandwich panel significantly enhance low frequency sound absorption and transmission loss. *Composite Structures* **182**, 1–11 (2017)
- [72] ISO 10534-2:1998(E), Determination of sound absorption coefficient and impedance in impedance tubes (1998)
- [73] Romero-García, V., Theocharis, G., Richoux, O., Pagneux, V.: Use of complex frequency plane to design broadband and sub-wavelength absorbers. *The Journal of the Acoustical Society of America* **139**(6), 3395–3403 (2016)
- [74] Dong, G., Liao, G., Liu, H., Kuang, G.: A review of the autoencoder and its variants: A comparative perspective from target recognition in synthetic-aperture radar images. *IEEE Geoscience and Remote Sensing Magazine* **6**(3), 44–68 (2018)
- [75] Tschannen, M., Bachem, O., Lucic, M.: Recent advances in autoencoder-based representation learning. *arXiv preprint arXiv:1812.05069* (2018)
- [76] Chen, L., Zhang, W., Nie, Z., Li, S., Pan, F.: Generative models for inverse design of inorganic solid materials. *Journal of Materials Informatics* **1**(1) (2021)
- [77] Loshchilov, I., Hutter, F.: Sgdr: Stochastic gradient descent with warm restarts. *arXiv preprint arXiv:1608.03983* (2016)
- [78] Komkin, A.I., Mironov, M.A., Bykov, A.I.: Sound absorption by a Helmholtz resonator. *Acoustical Physics* **63**(4), 385–392 (2017)
- [79] Li, D., Chang, D., Liu, B.: Enhanced low-to mid-frequency sound absorption using parallel-arranged perforated plates with extended tubes and porous material. *Applied Acoustics* **127**, 316–323 (2017)
- [80] Guo, J., Zhang, X., Fang, Y., Jiang, Z.: Wideband low-frequency sound absorption by inhomogeneous multi-layer resonators with extended necks. *Composite Structures* **260**, 113538 (2021)

- [81] Bucciarelli, F., Fierro, G.M., Meo, M.: A multilayer microperforated panel prototype for broadband sound absorption at low frequencies. *Applied Acoustics* **146**, 134–144 (2019)
- [82] Stinson, M.R.: The propagation of plane sound waves in narrow and wide circular tubes, and generalization to uniform tubes of arbitrary cross-sectional shape. *The Journal of the Acoustical Society of America* **89**(2), 550–558 (1991)
- [83] Huang, S., Zhou, E., Huang, Z., Lei, P., Zhou, Z., Li, Y.: Broadband sound attenuation by metaliner under grazing flow. *Applied Physics Letters* **118**(6), 063504 (2021)